Front. Energy 2022, 16(5): 852–861
https://doi.org/10.1007/s11708-021-0811-7

RESEARCH ARTICLE

Yonghuan LI, Wei SONG, Guang JIANG, Yue YANG, Hongmei YU, Zhigang SHAO, Fangwei DUAN, Yingxuan YANG

Ti_4O_7 supported IrO_x for anode reversal tolerance in proton exchange membrane fuel cell

Abstract Fuel starvation can occur and cause damage to the cell when proton exchange membrane fuel cells operate under complex working conditions. In this case, carbon corrosion occurs. Oxygen evolution reaction (OER) catalysts can alleviate carbon corrosion by introducing water electrolysis at a lower potential at the anode in fuel shortage. The mixture of hydrogen oxidation reaction (HOR) and unsupported OER catalyst not only reduces the electrolysis efficiency, but also influences the initial performance of the fuel cell. Herein, Ti_4O_7 supported IrO_x is synthesized by utilizing the surfactant-assistant method and serves as reversal tolerant components in the anode. When the cell reverse time is less than 100 min, the cell voltage of the MEA added with IrO_x/Ti_4O_7 has almost no attenuation. Besides, the MEA has a longer reversal time (530 min) than IrO_x (75 min), showing an excellent reversal tolerance. The results of electron microscopy spectroscopy show that IrO_x particles have a good dispersity on the surface of Ti_4O_7 and IrO_x/Ti_4O_7 particles are uniformly dispersed on the anode catalytic layer. After the stability test, the Ti_4O_7 support has little decay, demonstrating a high electrochemical stability. IrO_x/Ti_4O_7 with a high dispersity has a great potential to the application on the reversal tolerance anode of the fuel cell.

Keywords proton exchange membrane fuel cell (PEMFC), fuel starvation, cell reverse, reversal tolerance anode, oxygen evolution reaction

Received Jul. 16, 2021; accepted Sept. 27, 2021; online Jan. 10, 2022

Yonghuan LI, Guang JIANG, Yue YANG
Fuel Cell System and Engineering Laboratory, Key Laboratory of Fuel Cells and Hybrid Power Sources, Dalian Institute of Chemical Physics, Chinese Academy of Sciences, Dalian 116023, China; University of the Chinese Academy of Sciences, Beijing 100039, China

Wei SONG (✉), Hongmei YU, Zhigang SHAO (✉)
Fuel Cell System and Engineering Laboratory, Key Laboratory of Fuel Cells and Hybrid Power Sources, Dalian Institute of Chemical Physics, Chinese Academy of Sciences, Dalian 116023, China
E-mails: songwei05@dicp.ac.cn (Wei SONG); zhgshao@dicp.ac.cn (Zhigang SHAO)

Fangwei DUAN, Yingxuan YANG
State Grid Liaoning Electric Power Research Institute, Shenyang 110055, China

1 Introduction

Proton exchange membrane fuel cell (PEMFC) has attracted wide attention in recent years due to its advantage of high conversion efficiency, high power density, and environmentally friendliness [1]. However, its cost, performance, and durability are the three major challenges in the process of large-scale commercialization [2,3].

The supply of hydrogen may be delayed or insufficient when the fuel cell is operating under complicated conditions, such as start-up [4], rapid load change [5], and when flooded [6,7]. In particular, the anode potential increases rapidly to about 1.5 V or higher when fuel starvation happens in a cell of the stack. In this case, other reactions like water electrolysis and carbon corrosion will occur to provide protons and electrons for the current output [8,9]. The reaction formulas can be expressed as [6,10,11]

$$2H_2O \rightarrow O_2 + 4H^+ + 4e^-,$$
$$E^0 = 1.229\ \text{V (vs. SHE)}; \quad (1)$$

$$C + 2H_2O \rightarrow CO_2 + 4H^+ + 4e^-,$$
$$E^0 = 0.207\ \text{V (vs. SHE)}; \quad (2)$$

$$C + H_2O \rightarrow CO + 2H^+ + 2e^-,$$
$$E^0 = 0.518\ \text{V (vs. SHE)}. \quad (3)$$

It is well known that the reaction rate of carbon corrosion is much slower than that of water electrolysis [1,12,13]. Therefore, water electrolysis usually takes place first during cell reversal process. Unfortunately, the hydrogen oxidation reaction (HOR) catalyst like Pt/C will lose its function after a period of time due to the poisoning caused by carbon oxidation products [14–16]. Subsequently, an anode potential will rise rapidly attributing to the dominance of carbon corrosion [17]. The decay of carbon support would cause the aggregation or shedding of Pt particles, thus seriously damaging the anode catalytic layer (CL) [18]. The heat generated by carbon corrosion will lead to the formation of pinholes in proton exchange membrane [1]. In addition, the fuel and oxidant will mix in the reaction chamber, resulting in a catastrophic failure [19]. System control strategies are proposed in order to monitor the health of the stack system and find abnormalities in time, such as detecting the emitted CO_2 [8,9] and using it as an indicator to diagnose the abnormality of the system, detecting the localized anode potential [20,21], and monitoring the change in the stoichiometric ratio of the reactant gas [22], etc. However, these strategies require the support of additional systems so that the cost and complexity of the stack system will be increased. Reversal tolerance anode (RTA) is a reliable method based on materials to replace system strategies. The anode catalyst layer is usually doped with OER catalysts to extending the reaction time of water electrolysis in cell reverse, so as to alleviate the rate of carbon corrosion [23,24].

In recent years, a variety of OER catalysts have been used in the RTA, such as IrO_2 [1], RuO_2 [6], IrRu alloy [25,26], etc. Of these OER catalysts, IrO_2 has the best stability, and its activity is second only to RuO_2 [27–29]. Therefore, IrO_2 can decompose water for a long time at a relatively low potential. However, it is usually added directly into the anode in the form of particulate matter in most literature. In this case, IrO_2 may agglomerate in the catalytic layer so that it cannot protect all the carbon support [30]. Based on this situation, Roh et al. [30] deposited monodisperse IrO_2 on commercial Pt/C, and effectively improved the dispersion of IrO_2 in the catalytic layer. However, the preparation steps are cumbersome. Jang et al. [31] added IrO_2/C to the anode by improving the dispersion of IrO_2 on carbon, which showed less cell performance degradation than that of adding IrO_2 after frequent cell reverse. However, the additional carbon introduction would increase the possibility of corrosion. Consequently, it is necessary to improve the dispersion of IrO_2 in the catalytic layer and develop antioxidant catalyst supports at the same time. Ti_4O_7 has been widely regarded as a corrosion-resistant and electrically conductive material [32]. There are some reports utilizing Ti_4O_7 as a support material. For example, Ioroi and Yasuda [33] used Ti_4O_7 as the support of Pt, which greatly improved the reversal tolerance of the cell under the condition of fuel starvation. Won et al. [34] used Ti_4O_7 supported PtIr alloy as a bifunctional catalyst, showing excellent oxygen reduction reaction (ORR) and OER performance compared with single metal. However, there is no report on using Ti_4O_7-supported iridium oxide as the reversal tolerant components in the presence of Pt/C.

In this study, IrO_x/Ti_4O_7 was synthesized by utilizing the surfactant-assistant method. For comparison, IrO_x without support was prepared in the same way. The electrochemical performance of OER catalysts was characterized by half-cell and full cell tests. The dispersity of the catalysts which contribute to the electrolysis performance was analyzed by transmission electron microscopy (TEM), scanning electron microscope (SEM), and energy dispersive spectroscopy (EDS). In addition, the electrochemical stability of Ti_4O_7 in the three electrode system was studied. The results show that IrO_x particles have a good dispersity on the surface of Ti_4O_7 and IrO_x/Ti_4O_7 particles are uniformly dispersed on the anode catalytic layer, which make the reverse tolerance of MEA with IrO_x/Ti_4O_7 much better than MEA with IrO_x.

2 Experiment

2.1 Preparation of IrO_x and IrO_x/Ti_4O_7

The IrO_x/Ti_4O_7 was synthesized by the surfactant-assistant method [35]. Typically, 328 mg of Ti_4O_7 (Changsha Purong Chemical Engineering Inc.) was ultrasonically dispersed in 60.8 mL of distilled water (18.2 mΩ). Then, 153 mg of Pluronic® F127 (Sigma-Aldrich) was dissolved in the mixture and stirred for 30 min. After adding 626.3 mg of $H_2IrCl_6 \cdot xH_2O$ (Tianjin Jinbolan Fine Chemical Co., Ltd.), the mixture was vigorously stirring at 60°C for 5 h. After that, the sample was added with 12.2 mL of $NaBH_4$ solution (1 mol/L) at the same concentration as that of F127. Ultimately, the mixture was stirring overnight at 60°C for 12 h. After the reaction, the product was washed several times with anhydrous ethanol and dried at 60°C. The mass content of IrO_x in IrO_x/Ti_4O_7 is 32% (mass fraction). For comparison, the IrO_x without support was prepared in the same way.

2.2 Characterizations

The morphology of the synthesized catalysts was characterized by transmission electron microscopy (TEM, JEM 2100) at 120 kV. The cross-section morphology was observed by field emission scanning electron microscopy (SEM, JSM-7800F). Energy dispersive X-ray spectroscopy (EDS) mapping was conducted by the detectors on SEM at an accelerated voltage of 20 kV to observe the distributions of Pt, Ir, and Ti on the electrode surface. The crystal structure of the catalysts was characterized by X-ray diffraction (XRD, PANalytical Empyrean) with a Cu-

Kα tube. X-ray photoelectron spectroscopy (XPS, ESCALABXi) with an Mg anode was utilized to reveal the chemical state of the prepared IrO_x. The catalyst loading in terms of Ir content was measured via an inductively coupled plasma optical emission spectrometer (ICP-OES, 7300DV).

2.3 Electrochemical measurements

Electrochemical measurements were performed in the N_2-saturated 0.5 mol/L H_2SO_4 solution at 30°C with a rotating disk electrode (RDE) system in the traditional three electrode system, which consisted of a glassy carbon electrode (GCE, 0.1256 cm^2), a saturated calomel electrode (SCE), and a Pt tablet as the working, counter, and reference electrode, respectively. All potentials used in this study were calibrated by reversible hydrogen electrode (RHE). The catalyst ink was prepared by mixing 5 mg of powder, 1 mL of isopropyl alcohol (Aladdin), and 50 μL of Nafion solution (5%, Dupont). Then, 10 μL of the ink was deposited onto the GCE, drying naturally in air.

The stability of Ti_4O_7 was tested by potentiostatic method at 1.5 V for 5 h in a CHI 760 E electrochemical system. The linear sweep voltammetry (LSV) was carried out from 0 V to 1.4 V at 2 mV/s with a rotation rate of 1600 r/min, using the Gamry Interface 1000 E. Before the test, the catalyst was activated by cyclic voltammetry (CV) from 0 V to 1.2 V at 100 mV/s for 30 cycles.

2.4 MEA fabrication and single cell test

First, catalyst coated membrane (CCM) was prepared [36], and then MEA was prepared by hot pressing. Typically, the catalyst ink of cathode was prepared by mixing Pt/C (70% (mass fraction), Johnson Matthey) with isopropyl alcohol, deionized water, and Nafion solution. The specific composition of the anode catalyst is listed in Table 1. The Pt loadings of the cathode and anode were 0.4 and 0.2 mg/cm^2, respectively. The mass ratio of the ionomer/carbon (I/C ratio) was 0.7. The catalyst inks were directly sprayed on both sides of the Nafion 212 membrane. Finally, the MEA was fabricated by hot pressing the CCM with two gas diffusion layers (GDL) at 140°C, 0.1 MPa for 2 min. The effective area was 5 cm^2.

Table 1 Composition of catalysts in the anode

Catalyst/(mg·cm^{-2})	MEA-1	MEA-2	MEA-3
Pt/C	0.2	0.2	0.2
IrO_x	0	0.1	0
IrO_x/Ti_4O_7	0	0	0.3

The single cell test was conducted on a computer-controlled home-made test bench. The polarization curve (*I-V*) and the electrochemical impedance spectroscopy (EIS) were measured at 75°C, with a back pressure of 0.05 MPa (gauge pressure). The flow rates of fully humidified H_2 (anode) and air (cathode) were 120 and 800 mL/min, respectively. Before testing, all the single cells were activated for 4 h. The *I-V* curve was measured by KFM2030 (Kikusui, Japan). The EIS was measured by Gamry Interface 5000 E under the same condition of the *I-V* curve with the frequency ranging from 0.1 Hz to 10 kHz. The current density was kept at 0.2 A/cm^2.

The cell reversal test was conducted without back pressure at 75°C and the relative humidity (RH) of anode and cathode was both 100%. First, H_2 and air were supplied to the anode and cathode for about 30 min, respectively. Then, the H_2 was suddenly replaced by N_2. After that, a constant current of 0.2 A/cm^2 was supplied to the cell until the cell voltage reaches –2 V [6,11,27]. The schematic diagram of the voltage reversal test station is shown in Fig. 1. The *I-V* curve and EIS after the cell reversal test were performed. The reversal time is defined as the time that the voltage drops from 0 to –2 V.

3 Results and discussion

3.1 Physical characterizations of the catalysts

Physical characterizations of the catalysts were conducted by XRD, XPS, and TEM. The crystal structure of the catalysts was performed by XRD. Figure 2 depicts the XRD pattern of the synthesized IrO_x and IrO_x/Ti_4O_7. The two peaks in the spectrum of IrO_x are attributable to the most intense peak of the hollandite or rutile phases of IrO_2 [37]. It can be found that there is no obvious peak of Ir and IrO_2 in the spectrum of IrO_x/Ti_4O_7 compared to the standard JCPDS cards (JCPDS No. 15-0780; JCPDS No. 87-0715). These results indicate that the IrO_x is amorphous [38,39].

XPS was performed to investigate the electronic state of the Ir element. The XPS spectrum of Ir 4f for IrO_x and IrO_x/Ti_4O_7, as well as the full XPS spectrum of IrO_x/Ti_4O_7 is presented in Fig. S1 in Electronic Supplementary Material (ESM). Figures 3(a) and 3(b) manifest the fitted Ir 4f and O 1s spectra, respectively. Figure 3(a) shows the high resolution Ir 4f spectrum of IrO_x/Ti_4O_7. The two peaks correspond to the Ir $4f_{5/2}$ and Ir $4f_{7/2}$, respectively. Then, each peak was deconvoluted into two peaks for the analysis of Ir element on the IrO_x/Ti_4O_7 in detail. The most intense doublet at 62.38 and 65.28 eV can be attributed to Ir $4f_{7/2}$ and Ir $4f_{5/2}$, corresponding to the Ir^{3+}. The weaker doublet at 63.38 and 66.48 eV can be assigned to the Ir^{4+} [40–42]. According to the area integral results of each fitting curve, the content of Ir in different valence states is estimated. Ir^{3+} and Ir^{4+} account for 47% and 53% (atomic percentage), respectively. Therefore, the synthesized IrO_x/Ti_4O_7 is likely to provide a sufficient OER activity with a

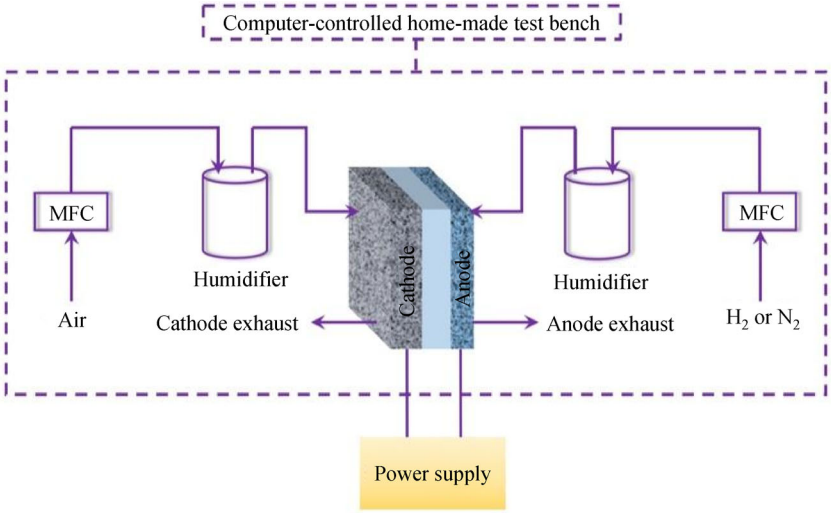

Fig. 1 Schematic diagram of voltage reversal test station.

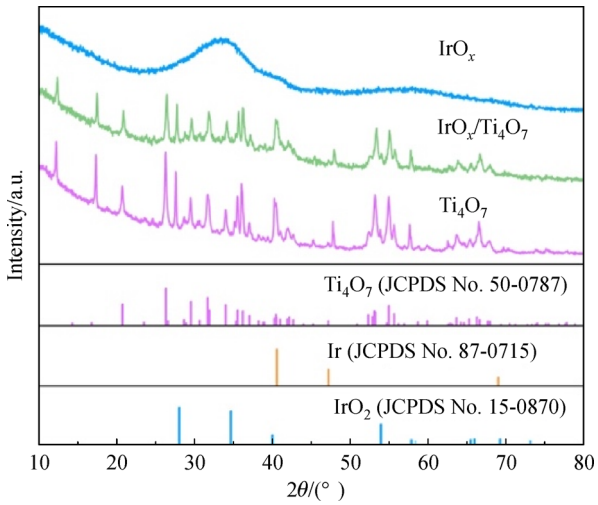

Fig. 2 XRD patterns of synthesized IrO_x, IrO_x/Ti_4O_7 and initial Ti_4O_7 with the standard card for IrO_2 and Ti_4O_7.

perfect durability due to the increased Ir^{4+} states [43]. Figure 3(b) exhibits the peaks of different kinds of oxygen in the XPS spectrum of O 1s. In the catalyst, about 91% (atomic percentage) of the oxygen exists in the form of metal oxide while the rest is surface species.

Figure 4 shows the TEM images and particle sizes of Ti_4O_7 and IrO_x/Ti_4O_7. Figure 4(a) is the image of Ti_4O_7 which has irregular shapes, such as particles and blocks. The particle size of Ti_4O_7 ranges from 80 nm to 150 nm. As shown in Fig. 4(c), IrO_x nanoparticles are well dispersed on the Ti_4O_7 (the red mark in the picture). The perfect dispersion is beneficial to improve the mass specific activity of the catalyst and the electrolysis efficiency compared to the form of aggregation. The particle size and distribution of IrO_x on the Ti_4O_7 are displayed in Fig. 4(d). The particle size of IrO_x ranges from 1 to 2 nm and the average particle size is 1.53 nm. Such a small particle size is due to the effect of Pluronic®F127, which plays a huge role as a template and stabilizer. Specifically, it can trigger seeds formation and control the size, shape and dispersion of IrO_x amorphous nanoparticles [35].

3.2 Electrochemical characterizations of the catalysts

The electrochemical stability of Ti_4O_7 was tested by utilizing the potentiostatic method at 1.5 V for 5 h. Figure S2 in ESM shows the CV curves of Ti_4O_7 before and after the stability test. As seen in Fig. S2 in ESM, there is no obvious redox peak in the initial CV curve, nor in that after the test. This shows that Ti_4O_7 has not been oxidized into TiO_2 after the potentiostatic test. Ti_4O_7 still maintains its original structure and conductivity. This means that the Ti_4O_7 has an excellent electrochemical stability at 1.5 V, which is expected to be seen in the reverse of fuel cell.

The electrochemical activity of synthesized catalysts was measured by LSV. The curves mainly reveal the performance of IrO_x and IrO_x/Ti_4O_7 between 1.4 V and 1.65 V (versus RHE). Figure 5(a) shows the OER activity of the catalysts. The overpotential of IrO_x is 303 mV (@ 10 mA/cm^2) while that of IrO_x/Ti_4O_7 is only 293 mV. This means that IrO_x/Ti_4O_7 can perform oxygen evolution reaction at a relatively low potential. As shown in Fig. 5(b), the mass specific activity (MA) of IrO_x at 1.6 V (versus RHE) is 90 mA/mg$_{Ir}$. The MA of IrO_x/Ti_4O_7 is 273 mA/mg$_{Ir}$, which is three times that of IrO_x. This can be attributed to the dispersion effect of IrO_x on Ti_4O_7, which leads to the exposure of more activity sites. The existence of Ti_4O_7 suppresses the aggregation of IrO_x to a certain extent. Besides, Ti_4O_7 reduces the amount of precious metal iridium under the condition of the same performance.

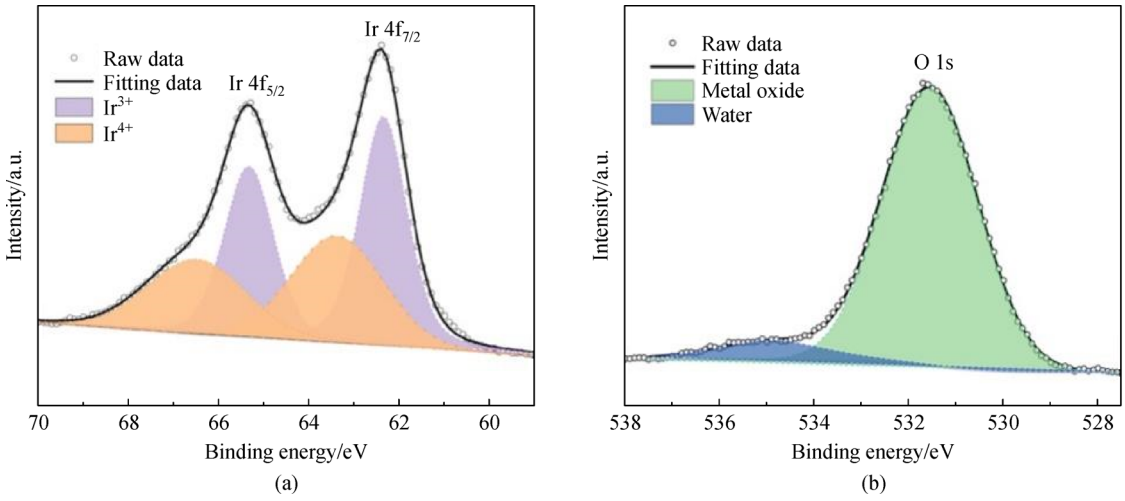

Fig. 3 XPS spectrum of IrO_x/Ti_4O_7.
(a) XPS spectrrum of Ir 4f; (b) spectrum of O 1s.

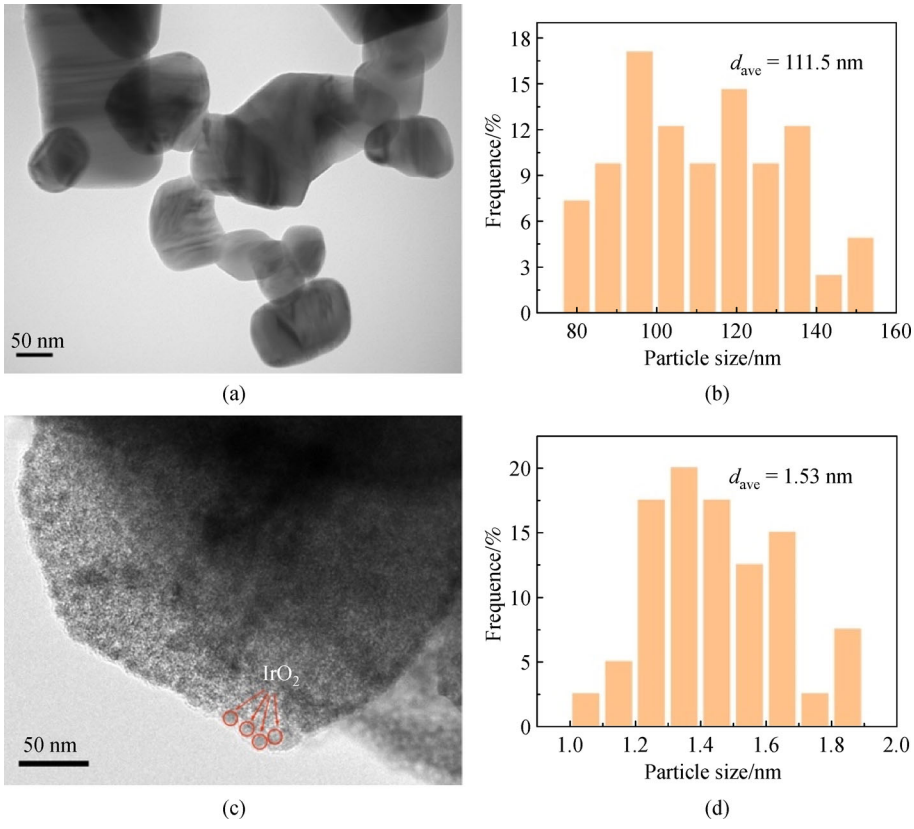

Fig. 4 TEM images and particle sizes.
(a) TEM image of Ti_4O_7; (b) particle size of Ti_4O_7; (c) TEM image of IrO_x/Ti_4O_7; (d) particle size of IrO_x on Ti_4O_7.

3.3 Performance of single cell

The result of the half-cell test indicates that the IrO_x/Ti_4O_7 has an excellent oxygen evolution activity and the Ti_4O_7 has a good chemical stability under an acidic condition. After this, the initial electrochemical performances of the two MEAs were studied, in which 0.1 mg/cm^2 IrO_x (MEA-2) and IrO_x/Ti_4O_7 (MEA-3) were added respectively. For comparison, the cell performance of the traditional Pt/C anode (MEA-1) is also given in Fig. 6, from which it can be observed that the initial performances of the anodes with the two self-made OER catalysts and that of the

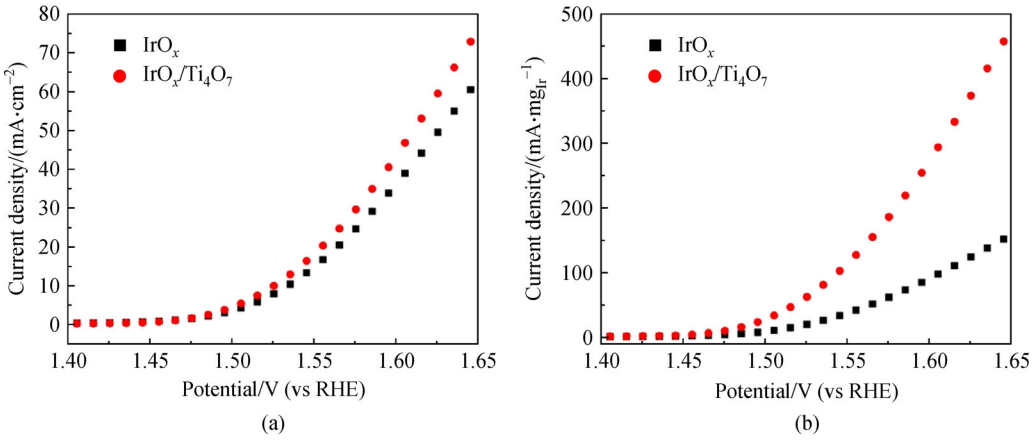

Fig. 5 OER activity of the catalysts.
(a) LSV curves of IrO_x and IrO_x/Ti_4O_7; (b) Ir-normalized LSV curves of IrO_x and IrO_x/Ti_4O_7.

traditional Pt/C without OER catalyst are different from each other. The *I-V* curves are shown in Fig. 6(a) and the performance parameters are presented in Fig. 6(b). At a current density of 1000 mA/cm^2, MEA-1 obtains the highest cell voltage (0.627 V) of the three MEAs, followed by MEA-2 (0.625 V). The cell voltage of MEA-3 is 0.618 V. Besides, the maximum power density of MEA-1, MEA-2, and MEA-3 are 743.4, 725.6, and 747.5 mW/cm^2, respectively. There is no obvious difference between the three MEAs at a current density range of less than 1200 mA/cm^2. However, the difference in cell voltage is obviously above 1200 mA/cm^2. The mass transfer problem of MEA-2 is most serious. This can be attributed to the addition of IrO_x into the anode catalyst layer of MEA-2. The resistance of electron transmission in the catalytic layer will be increased because of the poor conductivity of oxides. However, the performance of MEA-3 in the high current density region is normally worse than that of MEA-2 because it has a thicker catalytic layer. As shown in Figs. S3(a) and S3(b) in ESM, the anode catalytic layer of MEA-3 is 2.3 μm, which is 1.6 times that of MEA-2 (1.4 μm). On the contrary, MEA-3 has a better performance than MEA-2. This can be attributed to the excellent electrical conductivity of Ti_4O_7 [44] so that the adverse effect of thicker catalytic layer will be reduced. To sum up, there is no doubt that the introduction of OER catalysts into the anode catalyst layer will cause the initial performance of the cell to slightly decrease in the high current density region whether the OER catalyst is IrO_x or IrO_x/Ti_4O_7. The decrease of IrO_x/Ti_4O_7 is smaller than that of IrO_x because of the better electrical conductivity of Ti_4O_7 and the excellent dispersion of IrO_x.

3.4 Cell reversal tolerance of MEA

The cell reversal tests of the MEAs with OER catalysts were conducted. The voltage-time (*V-T*) curves during the cell reverse, the *I-V* curves, and EIS are presented in Fig. 7.

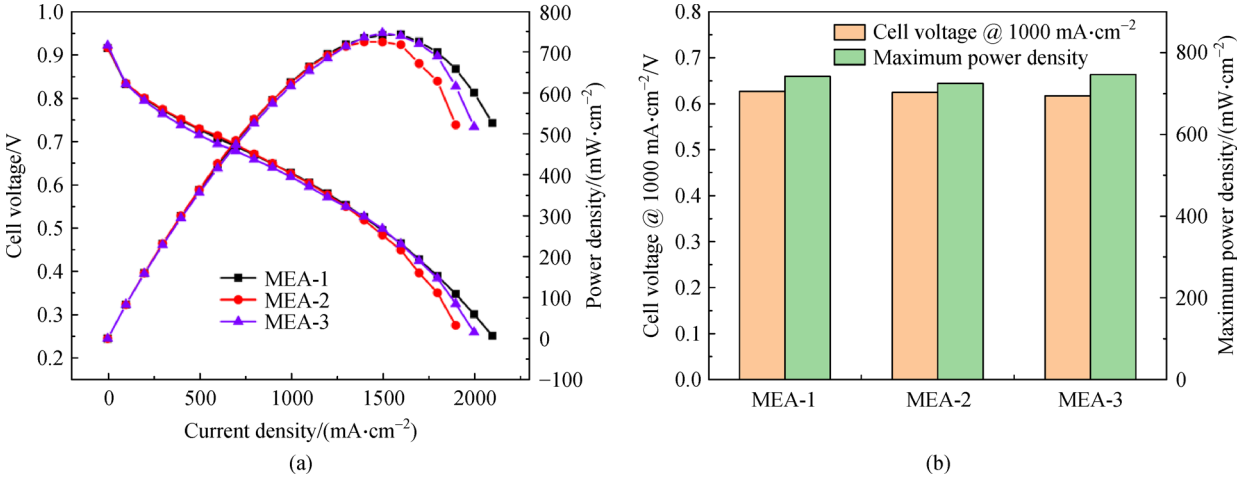

Fig. 6 Performance of the three MEAs.
(a) *I-V* curves of the three MEAs; (b) performance parameters of the three MEAs.

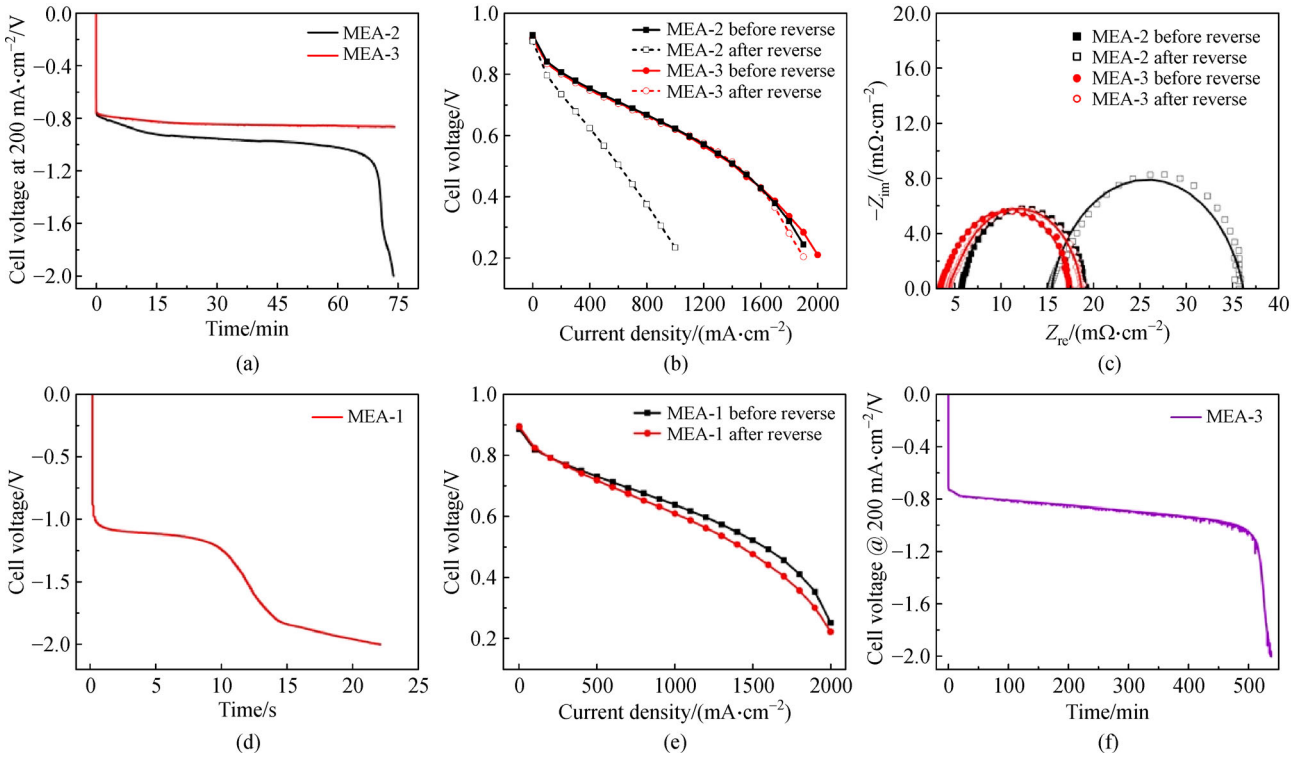

Fig. 7 Single cell performance of MEA-1, MEA-2 and MEA-3.

(a) Voltage-time curves of MEA-2 and MEA-3 during the cell reverse with the same time; (b) *I-V* curves of MEA-2 and MEA-3 before and after cell reverse; (c) EIS of MEA-2 and MEA-3; (d) voltage-time curve of MEA-1 during the cell reverse; (e) *I-V* curves of MEA-1 before and after cell reverse; (f) voltage-time curve of MEA-3 undergoing the entire cell reverse.

Figure 7(a) is the *V-T* curve of MEA-2 and MEA-3 during the cell reverse. After H_2 was switched to N_2, the residual H_2 in the pipeline and inside the cell was quickly exhausted and the cell voltage jumped below 0 V at the same time. As observed in Fig. 7(a), MEA-2 and MEA-3 have the same time of cell reverse (about 75 min). The voltage of MEA-2 during water electrolysis drops obviously while that of MEA-3 is relatively stable. This means that the stability of the water electrolysis reaction for MEA-3 is better than that of MEA-2. The *I-V* curves of MEA-2 and MEA-3 are tested after cell reverse, and the results are shown in Fig. 7(b). The voltage of MEA-3 has almost no attenuation after cell reverse. However, the voltage of MEA-2 at 1000 mA/cm^2 is attenuated by 62.5%. Because the stability of the OER for the IrO_x is worse than that of the IrO_x/Ti_4O_7, the efficiency of OER is gradually reduced, resulting in a more serious carbon corrosion. This can also be seen from EIS (Fig. 7(c)), the initial ohmic resistances (R_Ω, which is determined by the intercept of the real axis) at a high frequency of MEA-2 and MEA-3 are 5.8 and 3.5 mΩ·cm^2, respectively. After undergoing the cell reverse, the R_Ω of MEA-2 increases to 15.5 mΩ·cm^2, while that of MEA-3 is 4.4 mΩ·cm^2. Besides, the growth rate of the charge transfer resistances (R_{ct}) of MEA-2 and MEA-3 are 56.0% and 1.4%, respectively. Obviously, the anode catalytic layer of MEA-2 has suffered from a severe carbon corrosion, which leads to the destruction of catalytic layer structure and affects the charge transfer. To further prove the excellent reverse tolerance of MEA-3, the reverse tolerance performance of MEA-1 was tested, as shown in Figs. 7(d) and 7(e). Since the anode catalyst of MEA-1 is only Pt/C and its OER activity is very low, the reverse time is only 22 s. The *I-V* curves of the MEA before and after the cell reverse test are given in Fig. 7(e). The voltage attenuation at 1000 mA/cm^2 is 5.86%. Its reverse time is two orders of magnitude shorter than that of MEA-3, but the voltage attenuation is more serious. Therefore, compared with MEA-1, MEA-3 has an excellent reverse tolerance.

In addition, the total reverse time of MEA-3 is 530 min (Fig. 7(f)), which is about 7 times that of MEA-2 (75 min, Fig. 7(a)). The longer time is attributed to the excellent dispersion of IrO_x on Ti_4O_7. Based on this, the OER catalyst can expose more active sites, prolonging the reaction time of water electrolysis. SEM and EDS mapping images on the surface of the catalytic layer were obtained for the distribution of OER catalysts. Figure 8(a) is the image of MEA-2, in which the Ir element shows an obvious aggregation on the surface of the catalytic layer from the element mapping. Therefore, only a small area of carbon support can be protected. In contrast, Fig. 8(b) shows that the iridium is uniformly distributed on the

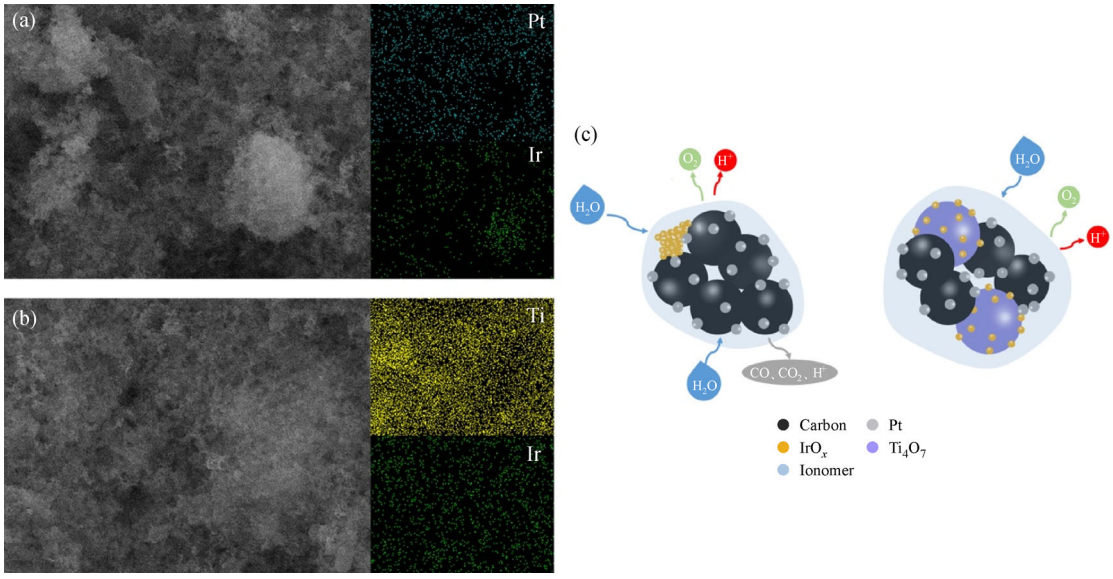

Fig. 8 Distribution of IrO_x and IrO_x/Ti_4O_7 in the catalyst layer.
(a) Element mapping of anode surface of MEA-2; (b) element mapping of MEA-3; (c) schematic diagram of the catalysts in the anode CL of MEA-2 and MEA-3.

surface of the catalytic layer of MEA-3, which can protect most of the carbon support. Figure 8(c) illustrates the distribution of the two catalysts in the CL. The result of EDS intuitively reveals the uniform distribution of IrO_x supported by Ti_4O_7 in the catalytic layer, which provides an evidence for the reason why MEA-3 has a longer time of water electrolysis. Ti_4O_7 supported IrO_x could provide a longer time of water electrolysis at a relatively stable voltage, which is beneficial to the reverse tolerance of the MEA.

4 Conclusions

In this study, Ti_4O_7 supported IrO_x with a small particle size of 1.53 nm was prepared by the surfactant-assistant method. As a catalyst support, Ti_4O_7 has shown an excellent electrochemical stability at 1.5 V. IrO_x supported on Ti_4O_7 can effectively reduce the amount of precious metal iridium and improve the catalytic efficiency for the RTA compared to the unsupported IrO_x. The reverse time of the prepared MEA with IrO_x/Ti_4O_7 in the anode has reached 530 min, which is 7 folds to that with IrO_x, indicating a better cell reverse tolerance under actual working conditions. This can be explained by the excellent dispersion of IrO_x on Ti_4O_7 and IrO_x/Ti_4O_7 on the anode catalytic layer. The initial cell performance only decreases by 1.4% at 1000 mA/cm^2 with the addition of IrO_x/Ti_4O_7 to the anode of the MEA for the superior conductivity of Ti_4O_7. Compared to the recently developed RTA based on carbon-free support, it is a desirable choice to add supported OER catalysts to the anode without sacrificing too much initial cell performance. In particular, support materials with a high conductivity and good corrosion resistance should be considered.

Acknowledgements This work was supported by the National Key Research and Development Program of China (No. 2019YFB1504502), and the Science and Technology Project of State Grid Corporation of China (SGLNDK00KJJS1900037).

Electronic Supplementary Material Supplementary material is available in the online version of this article at https://doi.org/10.1007/s11708-021-0811-7 and is accessible for authorized users.

References

1. Hong B K, Mandal P, Oh J G, et al. On the impact of water activity on reversal tolerant fuel cell anode performance and durability. Journal of Power Sources, 2016, 328: 280–288
2. Polagani R K, Suryawanshi P L, Gumfekar S P, et al. Ultrasound-assisted synthesis of Pt–Co/C bimetallic alloys for oxygen reduction in PEM fuel cells. Sustainable Energy & Fuels, 2018, 2(7): 1491–1499
3. Debe M K. Electrocatalyst approaches and challenges for automotive fuel cells. Nature, 2012, 486(7401): 43–51
4. Jang J, Sharma M, Choi D, et al. Boosting fuel cell durability under shut-down/start-up conditions using a hydrogen oxidation-selective metal-carbon hybrid core-shell catalyst. ACS Applied Materials & Interfaces, 2019, 11(31): 27735–27742
5. Huang Z, Shen J, Chan S H, et al. Transient response of performance in a proton exchange membrane fuel cell under dynamic loading. Energy Conversion and Management, 2020, 226: 113492
6. Zhou X, Ji H, Li B, et al. High-repetitive reversal tolerant performance of proton-exchange membrane fuel cell by designing a suitable anode. ACS Omega, 2020, 5(17): 10099–10105

7. Shen J, Xu L, Chang H, et al. Partial flooding and its effect on the performance of a proton exchange membrane fuel cell. Energy Conversion and Management, 2020, 207: 112537
8. Liang D, Shen Q, Hou M, et al. Study of the cell reversal process of large area proton exchange membrane fuel cells under fuel starvation. Journal of Power Sources, 2009, 194(2): 847–853
9. Taniguchi A, Akita T, Yasuda K, et al. Analysis of electrocatalyst degradation in PEMFC caused by cell reversal during fuel starvation. Journal of Power Sources, 2004, 130(1–2): 42–49
10. Zhou F, Andreasen S J, Kær S K, et al. Analysis of accelerated degradation of a HT-PEM fuel cell caused by cell reversal in fuel starvation condition. International Journal of Hydrogen Energy, 2015, 40(6): 2833–2839
11. Mandal P, Hong B K, Oh J G, et al. Understanding the voltage reversal behavior of automotive fuel cells. Journal of Power Sources, 2018, 397: 397–404
12. Lim K H, Lee W H, Jeong Y, et al. Analysis of carbon corrosion in anode under fuel starvation using on-line mass spectrometry in polymer electrolyte membrane fuel cells. Journal of the Electrochemical Society, 2017, 164(14): F1580–F1586
13. Hu L, Hong B K, Oh J G, et al. Robust operation of fuel cell systems in subfreezing conditions: a material-based solution to achieve better anode durability. ACS Applied Energy Materials, 2019, 2(10): 7152–7161
14. Cai C, Rao Y, Zhou J, et al. Carbon corrosion: a novel termination mechanism of the water electrolysis plateau during voltage reversal. Journal of Power Sources, 2020, 473: 228542
15. Moore C E, Eastcott J, Cimenti M, et al. Novel methodology for *ex situ* characterization of iridium oxide catalysts in voltage reversal tolerant proton exchange membrane fuel cell anodes. Journal of Power Sources, 2019, 417: 53–60
16. Joo T, Hu L, Hong B K, et al. On the origin of deactivation of reversal-tolerant fuel cell anodes under voltage reversal conditions. Journal of Power Sources, 2020, 472: 228439
17. Zhao J, Tu Z, Chan S H. Carbon corrosion mechanism and mitigation strategies in a proton exchange membrane fuel cell (PEMFC): a review. Journal of Power Sources, 2021, 488: 229434
18. Ghosh S, Ohashi H, Tabata H, et al. In-plane and through-plane non-uniform carbon corrosion of polymer electrolyte fuel cell cathode catalyst layer during extended potential cycles. Journal of Power Sources, 2017, 362: 291–298
19. Lü W, Liu Z, Wang C, et al. The effects of pinholes on proton exchange membrane fuel cell performance. International Journal of Energy Research, 2011, 35(1): 24–30
20. Lauritzen M V, He P, Young A P, et al. Study of fuel cell corrosion processes using dynamic hydrogen reference electrodes. Journal of New Materials for Electrochemical Systems, 2007, 10(3): 143–145
21. Baumgartner W R, Parz P, Fraser S D, et al. Polarization study of a PEMFC with four reference electrodes at hydrogen starvation conditions. Journal of Power Sources, 2008, 182(2): 413–421
22. Chen H, Zhao X, Zhang T, et al. The reactant starvation of the proton exchange membrane fuel cells for vehicular applications: a review. Energy Conversion and Management, 2019, 182: 282–298
23. Atanasoski R T, Cullen D A, Vernstrom G D, et al. A materials-based mitigation strategy for SU/SD in PEM fuel cells: properties and performance-specific testing of IrRu OER catalysts. ECS Electrochemistry Letters, 2013, 2(3): F25–F28
24. Knights S D, Colbow K M, St-Pierre J, et al. Aging mechanisms and lifetime of PEFC and DMFC. Journal of Power Sources, 2004, 127(1–2): 127–134
25. Kim T Y, Lee S W, Pak C. Optimization of carbon-supported Ir–Ru alloys for polymer electrolyte fuel cell anodes under cell reversal. Journal of Industrial and Engineering Chemistry, 2020, 85: 87–93
26. You E, Min M, Jin S A, et al. Highly durable, cost-effective, and multifunctional carbon-supported IrRu-based catalyst for automotive polymer electrolyte fuel cell anodes. Journal of the Electrochemical Society, 2018, 165(6): F3094–F3099
27. Wang J, Zhou X, Li B, et al. Highly efficient, cell reversal resistant PEMFC based on PtNi/C octahedral and OER composite catalyst. International Journal of Hydrogen Energy, 2020, 45(15): 8930–8940
28. Kötz R, Lewerenz H J, Brüesch P, et al. Oxygen evolution on Ru and Ir electrodes. Journal of Electroanalytical Chemistry and Interfacial Electrochemistry, 1983, 150(1–2): 209–216
29. Trasatti S. Electrocatalysis in the anodic evolution of oxygen and chlorine. Electrochimica Acta, 1984, 29(11): 1503–1512
30. Roh C W, Kim H E, Choi J, et al. Monodisperse IrO_x deposited on Pt/C for reversal tolerant anode in proton exchange membrane fuel cell. Journal of Power Sources, 2019, 443: 227270
31. Jang I, Hwang I, Tak Y. Attenuated degradation of a PEMFC cathode during fuel starvation by using carbon-supported IrO_2. Electrochimica Acta, 2013, 90: 148–156
32. Krishnan P, Advani S G, Prasad A K. Magneli phase $Ti_n O_{2n-1}$ as corrosion-resistant PEM fuel cell catalyst support. Journal of Solid State Electrochemistry, 2012, 16(7): 2515–2521
33. Ioroi T, Yasuda K. Highly reversal-tolerant anodes using Ti_4O_7-supported platinum with a very small amount of water-splitting catalyst. Journal of Power Sources, 2020, 450: 227656
34. Won J E, Kwak D H, Han S B, et al. PtIr/Ti_4O_7 as a bifunctional electrocatalyst for improved oxygen reduction and oxygen evolution reactions. Journal of Catalysis, 2018, 358: 287–294
35. Li G, Yu H, Wang X, et al. Highly effective $Ir_xSn_{1-x}O_2$ electrocatalysts for oxygen evolution reaction in the solid polymer electrolyte water electrolyser. Physical Chemistry Chemical Physics, 2013, 15(8): 2858–2866
36. Wilson M S, Gottesfeld S. Thin-film catalyst layers for polymer electrolyte fuel cell electrodes. Journal of Applied Electrochemistry, 1992, 22(1): 1–7
37. Lee Y, Suntivich J, May K J, et al. Synthesis and activities of rutile IrO_2 and RuO_2 nanoparticles for oxygen evolution in acid and alkaline solutions. Journal of Physical Chemistry Letters, 2012, 3(3): 399–404
38. da Silva G C, Perini N, Ticianelli E A. Effect of temperature on the activities and stabilities of hydrothermally prepared IrO_x nanocatalyst layers for the oxygen evolution reaction. Applied Catalysis B: Environmental, 2017, 218: 287–297
39. Siracusano S, Baglio V, D'Urso C, et al. Preparation and characterization of titanium suboxides as conductive supports of IrO_2 electrocatalysts for application in SPE electrolysers. Electrochimica Acta, 2009, 54(26): 6292–6299
40. Wei G, Wang Y, Huang C, et al. The stability of MEA in SPE water electrolysis for hydrogen production. International Journal of

Hydrogen Energy, 2010, 35(9): 3951–3957
41. Pfeifer V, Jones T E, Velasco Vélez J J, et al. The electronic structure of iridium oxide electrodes active in water splitting. Physical Chemistry Chemical Physics, 2016, 18(4): 2292–2296
42. Badam R, Hara M, Huang H H, et al. Synthesis and electrochemical analysis of novel IrO_2 nanoparticle catalysts supported on carbon nanotube for oxygen evolution reaction. International Journal of Hydrogen Energy, 2018, 43(39): 18095–18104
43. Abbott D F, Lebedev D, Waltar K, et al. Iridium oxide for the oxygen evolution reaction: correlation between particle size, morphology, and the surface hydroxo layer from operando XAS. Chemistry of Materials, 2016, 28(18): 6591–6604
44. Senevirathne K, Hui R, Campbell S, et al. Electrocatalytic activity and durability of Pt/NbO_2 and Pt/Ti_4O_7 nanofibers for PEM fuel cell oxygen reduction reaction. Electrochimica Acta, 2012, 59: 538–547